PPPL-2560

PPPL-2560

UC-426

LOCAL CARBON DIFFUSION COEFFICIENT MEASUREMENT IN THE S-1 SPHEROMAK

By

R.M. Mayo, F.M. Levinton, D.D. Meyerhofer,
T.K. Chu, S.F. Paul, and M. Yamada

OCTOBER 1988

PLASMA
PHYSICS
LABORATORY

PRINCETON UNIVERSITY
PRINCETON, NEW JERSEY

PREPARED FOR THE U.S. DEPARTMENT OF ENERGY,
UNDER CONTRACT DE-AC02-76-CHO-3073.

Printed in the United States of America

Available from:

National Technical Information Service
U.S. Department of Commerce
5285 Port Royal Road
Springfield, Virginia 22161

Price Printed Copy $__*__; Microfiche $4.50

*Pages	NTIS Selling Price
1-25	$7.00
25-50	$8.50
51-75	$10.00
76-100	$11.50
101-125	$13.00
126-150	$14.50
151-175	$16.00
176-200	$17.50
201-225	$19.00
226-250	$20.50
251-275	$22.00
276-300	$23.50
301-325	$25.00
326-350	$26.50
351-375	$28.00
376-400	$29.50
401-425	$31.00
426-450	$32.50
451-475	$34.00
476-500	$35.50
500-525	$37.00
526-550	$38.50
551-575	$40.00
567-600	$41.50

For documents over 600 pages, add $1.50 for each additional 25-page increment.

PPPL--2560

DE89 004621

Local Carbon Diffusion Coefficient Measurement in the $S-1$ Spheromak

R. M. Mayo[†], F. M. Levinton[‡], D. D. Meyerhofer[‡], T. K. Chu, S. F. Paul, and M. Yamada

Princeton University,

Plasma Physics Laboratory,

Princeton, New Jersey 08544

United States of America

Abstract

The local carbon diffusion coefficient was measured in the $S-1$ spheromak by detecting the radial spread of injected carbon impurity. The radial impurity density profile is determined by the balance of ionization and diffusion. Using measured local electron temperature T_e and density n_e, the ionization rate is determined from which the particle diffusion coefficient is inferred. The results found in this work are consistent with Bohm diffusion. The absolute magnitude of $D_\perp$ was determined to be $(4 \sim 6) \times D_{Bohm}$.

[†]Purdue University, West Lafayette, IN 47907

[‡]On assignment from JAYCOR, Torrance, CA 90503

[‡]Present address: Department of Mechanical Engineering, Hopeman Hall, University of Rochester, Rochester NY 14627

1. Introduction

The spheromak [1] is a toroidal magnetic confinement plasma device which has received considerable attention in recent years. Because the spheromak plasma generates most of its own confining fields, there is no need for intrusive toroidal field coils that link the plasma. Thus, a simply closed vessel geometry is employed which greatly enhances the spheromak reactor potential. In addition, the spheromak plasma has poloidal and toroidal fields which are of approximately equal magnitudes. This is a consequence of the *force-free* equilibrium condition ($\vec{j} \times \vec{B} = \nabla p \sim 0$) investigated by Rosenbluth and Bussac[1].

It has been observed that spheromak plasmas may deviate from the force-free state. They may then tend to relax so that the force-free state is once again achieved, as predicted by Taylor[2-4]. Concomitant with this phenomenon of relaxation is the possibility of enhanced particle and energy transport. The purpose of this work is to directly measure the local particle transport coefficient, $D_\perp$, and compare this with classically predicted values.

Many methods for such measurements have been considered previously. A review of some of these is given in Ref. [5]. Methods like H_α monitoring and working gas puffing not only have the disadvantage of providing only global τ_p estimates, but have inherent difficulties associated with large neutral densities outside the $S \sim 1$ separatrix and large transit times compared to plasma lifetimes, respectively. Similar time scale problems exist with laser blowoff techniques. In situ impurity studies rely to a large degree on computer modeling of transport phenomenon and would again provide only global information by virtue of broad impurity profiles created by high transport rates in the $S \sim 1$ device.

For this work we have chosen a scheme similar to that of Levinton and Meyerhofer[5] and have extended the method to higher temperature plasmas. Previous results in the Proto-$S = 1$, C spheromak[6] have revealed that perpendicular particle transport occurs at a rate of 5 times Bohm over a limited parameter range. Here we have made measurements in a plasma with a larger range of magnetic field 0.9 – 2.5 kG and electron temperature

8 – 65 eV. To explore this extended parameter region we have developed a new method of *steady-state* impurity injection. The technique involves injecting impurities locally in the plasma (near the magnetic axis) by means of a graphite tipped probe. The radial diffusion of CII (spectroscopic notation) is followed spectroscopically using a multichord system which allows entire spatial emission profiles to be recorded on a single discharge. The balance between diffusion of CII particles and ionization to $CIII$ determines the width of the spatial emission profile about the injection point.

The diagnostic technique will be described in Section 2. In Section 3, the analytic methods used for calculating $D_\perp$ from the emission profiles will be presented. Finally, the results and scaling of $D_\perp$ with plasma parameters will be discussed in Section 4.

2. S – 1 Experimental Conditions and Diffusion Measurement Diagnostic

The S – 1 device and major components have been described previously [7,8], as well as the method of programmed formation [9]. In the present experiment, discharges were produced to provide global stability to tilt and shift modes[10] by a pair of passive conducting cones. Enhanced stability provided by these funnel (cone) stabilizers allows for transport study which has not been previously possible on this machine. The S – 1 device and spark probe diagnostic are shown schematically in Fig. 1.

2.1. Plasma Conditions

By charging the programmed poloidal and toroidal field producing capacitor banks to 8 – 14 kV, spheromak plasmas were created with toroidal plasma currents from 80 kA to 180 kA. The peak magnetic field in the plasma ranged from 1.0 – 2.5 kG. Hydrogen fill gas was puffed into the vessel several seconds before discharge initiation to a pressure of ~ 5 mTorr. This operation produced plasmas with electron densities of $0.5 - 1.7 \times 10^{14}$ cm^{-3} and electron temperatures ranging from 8 – 65 eV. The typical volume-averaged beta, $\langle\beta\rangle_{vol}$,

is 2.8 – 7.5%. These spheromak plasmas typically lasted from 0.5 – 0.7 *ms*. The time from $t = 0$ to $\sim 270\ \mu s$ is the plasma breakdown and formation phase. After formation, the spheromak equilibrium is seen to approach a *Taylor* state [9]. Low current discharges tend to remain close to this state for much of the discharge lifetime until termination, usually due to an $n = 1$ mode. In higher current discharges, however, the toroidal current density and electron temperature are seen to peak later in time (300 – 360 μs) [11]. This deviation from the Taylor state is usually followed by a sudden relaxation of the plasma to an equilibrium which is once again near the Taylor state. This relaxation is characterized by a noticeable flattening of the toroidal current density and electron temperature profiles. It has been conjectured [11] that at this time of relaxation, confinement is degraded. It will be shown later that confinement actually begins to degrade well before the relaxation time and that transport rates are continually increasing up to the relaxation time.

2.2. *Carbon Injection Diagnostic*

The D_α measurement diagnostic has been adopted and modified from that previously described[5]. We inject a small, localized source of carbon impurity directly into the main body of the plasma. The injection point was in the midplane ($z = 0$) and at R (major radius) positions of $R = 33\ cm$ and 42 *cm* (Fig. 2). The magnetic axis for these plasmas during the diffusion measuring time ranged between 45 and 55 *cm*, while the minor radius was $\sim 25\ cm$. The injection probe consists of two graphite electrodes connected to a 15 kV, 2 μF capacitor bank assembly (see Fig. 1) vacuum sealed in a 3/8" (O.D.) stainless steel tube. Carbon may be injected as a time dependent source by discharging the capacitor bank ($\sim 2\ \mu s$ quarter wave rise time) through the graphite electrodes. Carbon is also injected continuously by the interaction of the plasma with the probe tips. This allows a nearly steady-state injection during the discharge and provides an independent method of analysis. It also allows determination of the diffusion constant in higher temperature ($\gtrsim 10\ eV$) plasmas where the pulse-injected sources quickly ($< 10\ \mu s$) disappear by ionization.

The radial emission profiles for CII are recorded on a single shot using an Optical Multichannel Analyzer (OMA) system [12]. The imaging optics consist of one 1-1/2" simple convex quartz lens, f/2. The lens is mounted between the fiber ferrule and the quartz window (see Fig. 2) so that the image of the fibers is focussed at the midplane of the machine ($\sim 1\ m$ from the window) with a 15 cm radial spread centered at the spark probe. A 12 mm wide UV-grade quartz fiber optic bundle is used to couple the focusing optics at the $S-1$ machine to the spectrometer in an RF-shielded room. The guide consists of 50 - 200 μm diameter fused silica fibers individually clad in 40 μm silicon. The 10 m long guide is protected by a corrugated plastic sheath and the ends are mounted in plastic ferrules in a coherent line. Guide transmission is acceptable down to $\sim 250\ nm$ at which the attenuation approaches 1 db/m and the transmission drops to $\lesssim 1\%$.

The spectrometer is an ISA-HR320 high throughput 0.32 m Czerny-Turner f/4.8 instrument. With a 600 g/mm holographic grating, a resolution of ~ 2 A and a nominal range of 625 A can be achieved. This large range allows for the simultaneous detection of CII (4267 A) and $CIII$ (4647 A). The instrumental resolution, however, is insufficient to measure Doppler shifts or broadening.

The detector is a PARC 1254 silicon intensified target vidicon consisting of a 512×512 array of photocathode elements with an active area of 12.5 mm by 12.5 mm and a resolution of ± 2 A channels. This two-dimensional detector array is used to record plasma emission as a function of wavelength and radial position. In addition to being placed in an RF-shielded room $\sim 8\ m$ from the $S-1$ machine, the EMI sensitive electronics are placed in a soft iron sleeve to reduce deflection. The detector is also equipped with a PARC 1211 high voltage pulse generator and a PARC 1216 detector controller to control gating and data transfer to the VAX/VMS computer system. The minimum gate time for the detector is 40 ns although 5 - 20 μs is typically required to collect sufficient light to resolve the line spectra above background. Since high time resolution is required for the carbon injection experiment, 5 - 10 μs gate times were used throughout. The readout time for the detector is $\sim 500\ ms$

so that only one gating could be made per discharge. The shot-to-shot reproducibility was determined to be quite good ($\lesssim 14\%$) [12] so that large errors were not introduced in shot-by-shot scanning.

Two LeCroy 8201 memory modules are used in each gating. One module is filled $\sim 1\,s$ before the discharge to record the background light levels which are later subtracted from the plasma emission recorded during the shot in the other memory module. An example spectral emission trace (with background subtracted) for one radial position of a typical carbon injection discharge is shown in Fig. 3a.

A multipoint Thomson Scattering diagnostic [13,14] measures the local values of T_e and n_e at 5 to 10 spatial positions across the plasma radius, which are used to calculate the CII ionization rate. Ionization rates are taken from Bell et al. [15]. Local magnetic field strengths in the location of the injection probe were measured by a linear array of pickup loops [16] encased in stainless steel tubing and inserted into the spheromak midplane.

3. Measurement Technique and Analytic Methods

3.1. Measurement Technique and Assumptions

Since the injected source is in the plasma midplane, the radial direction is the $\nabla\psi$ direction (ψ is the poloidal flux function). Hence, the radial evolution of the carbon impurity is determined by perpendicular transport alone. The parallel diffusion coefficient, $D_\parallel$, cannot be inferred from this measurement as has been done on a similar experiment on Proto $S-1/C$ [5] since the focusing optics cannot be moved to other toroidal locations around the $S-1$ machine.

As mentioned earlier, two injection schemes have been utilized, the pulsed injection and the steady-state injection methods. The equivalence of these in determining $D_\perp$ will be demonstrated later. In reality, the steady-state source is always active even during pulsed injection since the probe injects continuously through plasma particle bombardment.

However, the emission obtained during pulsed injection is substantially larger than the steady-state emission, so the two sources are easily distinguished. In the pulsed injection method, approximately 5 - 6 kA of current flows between the graphite probe tips producing a local dipole field of nearly 20 kG. This represents a large local perturbation during the pulse. Hence, the details of the pulsed injection will not be modeled. Only after the probe current decays to zero will this data be analysed.

In both injection methods, the presence of the probe in the plasma and the increased impurity density due to injection cause insignificant perturbations to the plasma. Figure 3a shows the carbon emission with the injection probe in the machine and Fig. 3b is a similar discharge with the probe out of the machine. The local injected carbon density is substantially greater than the background levels, although the global carbon concentration did not increase significantly. There was no measurable reduction in the local electron temperature by the impurity injection. This is consistent with the large values of parallel electron thermal conduction expected [6]. In addition, similar diffusion coefficients were obtained when using both the steady-state and pulsed injection techniques, the latter method locally introduces almost an order of magnitude more carbon initially.

It is evident, from a consideration of the ion thermal speed $v_{th_i} = \sqrt{\frac{2T_i}{m_i}} \sim 3.3 \times 10^4\ m/s$ for carbon at $T_i = T_e \simeq 70\ eV$ (the highest electron temperature observed in this experiment) that it would take a time longer than the discharge lifetime for the injected carbon to fill an entire flux surface. In addition, perpendicular diffusion and ionization ensure that the only observable impurity concentration remains in the vicinity of the probe. Therefore, the impurity confinement is determined by the local magnetic field near the injection point rather than the entire flux surface. Furthermore, it is assumed that the observed transport may be described by a single quantity, $D_\perp$, while looking in the plane of the probe (i.e., $z = 0$).

The gradient scale lengths and time scales for change in plasma parameters in the seed

$S \gg 1$ plasma are long compared to those of the injected carbon. Therefore, it is assumed that the diffusion coefficient is constant during the short observation time ($5 \sim 10\ \mu s$) in the steady-state method and during the temporal evolution directly following the pulsed injection. The justification of the latter condition lies in the observation of approximately constant (in time) electron temperatures in $S \sim 1$ plasmas for low voltage discharges ($\lesssim 10\ eV$), the only condition where the pulsed technique may be employed.

Experimentally it has been determined that all the injected carbon is initially in the CII charge state. This has been verified by discharging the probe in vacuum, neutral fill (usually H_2 or N_2), and in low voltage plasmas. In all cases only CII was observed. ($CIII$ was observed in the low voltage plasma case but not above the normal background.) Hence, it is assumed that the source term is that of CII alone. This assertion is of substantial consequence since it removes the need to model neutral transport.

It is also assumed that in the vicinity of the injection probe the electron temperature and density are spatially constant. The ionization rates then become constants in the rate equations and the emission profiles may be regarded as relative impurity density profiles. The constant n_e assumption is quite well justified based on laser Thomson Scattering. In the case of T_e some profile peaking does appear in the higher voltage discharges. However, effects of non-uniform T_e profiles alter the analysis only when $T_e \lesssim E_{ex}, E_I$ (the excitation and ionization energies, respectively). These are 20 and 24.4 eV for CII at 4267 Å so there will only be important profile effects when T_e is low ($\lesssim 20\ eV$). The electron temperature typically takes on these values in the case of low voltage discharges where the profiles tend to be flat anyway. Hence, T_e profile effects are expected to be minor.

Finally, for the steady-state method it will be assumed that the charge states CII and $CIII$ have reached equilibrium determined by electron impact ionization and cross field transport. Because the observation times are long after the plasma breakdown ($\sim 250 - 400\ \mu s$) and ionization times are short ($1 - 10\ \mu s$), this is a good assumption. The

effects of recombination are assumed to be negligible on the time scales of the discharge. Excitation is assumed to occur between the ground state and the upper level of the transition being studied. This is a good assumption for the relatively low electron densities in this experiment since collision times are much longer than the decay times of most excited states (except for metastable states). The above assumptions also apply to the pulsed injection method, except that charge state equilibrium is not achieved until well after the probe firing time. The temporal evolution of the charge state densities must be followed in this case.

3.2. *Analytic Solutions*

The analysis of the emission profile data proceeds by solving the impurity continuity equation.

$$\frac{\partial n_{II}(\vec{x},t)}{\partial t} = D_{\perp}\nabla^2 n_{II}(\vec{x},t) - \langle\sigma v\rangle_{II,III} n_e n_{II}(\vec{x},t) + S(\vec{x},t) \quad . \tag{1}$$

Here $n_{II}(\vec{x},t)$ is the CII density, $\langle\sigma v\rangle_{II,III}$ is the electron impact ionization rate coefficient from CII to $CIII$, and $S(\vec{x},t)$ is the CII source term. This model ignores electron density gradients and assumes that the injected ion density gradients drive the diffusion. In particular, it is collisions between carbon ions and protons which are of interest. It is this fact that allows the transport term to be expressed as depending on the individual charge state density only. The source term $S(\vec{x},t)$ is found by discharging the carbon probe in H_2 neutral fill gas and in low T_e plasma discharges. A sample source emission profile for CII at 4267 A is shown in Fig. 4 with a superimposed gaussian curve

$$S(\vec{x},t) = C\ exp(-r^2/r_o^2) \quad , \tag{2}$$

where $r_o = 0.83\ cm$. The parameter r_o in Eq. (2) was determined from the average of many such discharges and will be used in the CII source expression throughout. Equation (1) can be simplified to one dimension

$$\frac{\partial n_{II}(r,t)}{\partial t} = D_{\perp}\frac{\partial^2 n_{II}(r,t)}{\partial r^2} - \langle\sigma v\rangle_{II,III} n_e n_{II}(r,t) + A\ exp(-r^2/r_o^2)\delta(t) \quad , \tag{3}$$

and may be solved by the method of Fourier transforms to yield

$$n_{II}(r,t) = \frac{Ar_o e^{-D_\perp \alpha^2 t}}{\sqrt{r_o^2 + 4D_\perp t}} exp(-\frac{r^2}{r_o^2 + 4D_\perp t}) \quad , \tag{4}$$

where $\alpha^2 = \frac{\langle \sigma v \rangle_{II,III} n_e}{D_\perp}$ so that $\alpha^2 D_\perp = \frac{1}{\tau_{ion}}$, the ionization rate for CII. The t in Eq. (4) refers to the time after firing the probe (i.e., $t = 0$, the time when the spark current turns off).

To quantify emission profiles obtained during plasma discharges when the probe capacitor bank had not been fired, we now imagine a time-independent CII continuity equation of the form

$$0 = D_\perp \frac{\partial^2 n_{II}(r)}{\partial r^2} - \langle \sigma v \rangle_{II,III} n_e n_{II}(r) + A\, exp(-r^2/r_o^2) \quad . \tag{5}$$

Equation (5) is assumed to be a steady-state equation only during the gating time of the instrument (5 - 10 μs). All the coefficients, including the source term, are assumed to be constant during this short time, a valid approximation in the present experiment. To follow the time history of the discharge, we gate at varied times on a shot-by-shot basis. The coefficients may vary on times long with respect to the gating time. This is accounted for by recording T_e and n_e at times in the discharge corresponding to detector gating times. As before, we employ the method of Fourier transforms to Eq. (5). The steady-state solution for the $n_{II}(r)$ profile is

$$n_{II}(r) = \frac{Ar_o\sqrt{\pi}}{4\alpha D_\perp} e^{\alpha^2 r_o^2/4} \{ e^{-\alpha r}[1 + erf(\frac{r}{r_o} - \frac{\alpha r_o}{2})] + e^{\alpha r}[1 - erf(\frac{r}{r_o} + \frac{\alpha r_o}{2})] \} \quad , \tag{6}$$

where $erf(x)$ is the error function[17]. In the limit $\alpha r_o \ll 1$, the solution becomes

$$n_{II}(r) \sim \frac{Ar_o\sqrt{\pi}}{2\alpha D_\perp} e^{-\alpha|r|} \quad , \tag{7}$$

which is exactly the solution one would obtain by using a spatial delta function source term in Eq. (5). From this limiting form it can easily be shown that

$$D_\perp = \langle \sigma v \rangle_{II,III} n_e (\frac{r_{1/2}}{\ln 2})^2 = \frac{r_{1/2}^2}{(\ln 2)^2 \tau_{ion}} \quad , \tag{8}$$

where $r_{1/2}$ is the half-width of the profile. This is exactly the result that would be expected for ionization balanced diffusion at steady-state. Equations (7) and (8) have a convenient and simple form, yet they cannot be used in practice. The source width, r_o, is not negligible on the length scale of $r_{1/2}$ and, therefore, cannot be ignored. Equation (6) must be used.

3.3. *Evaluating $D_\perp$ from Experimental Emission Profiles*

From the derivations of the previous Section, we can now evaluate $D_\perp$ from the CII measured emission profiles. Two methods were developed so that independent measures of the transport quantity may be obtained as well as ensuring the applicability of at least one method over the entire range of plasma parameters. We may proceed from the formalism of Eq. (4) by analyzing data like that presented in Fig. 5. Here the peak of the CII emission profile is followed in time from the probe firing time (250 μs). The open circles represent the emission peaks observed after the probe was fired while the closed circles are the profile peaks for the non-firing, steady-state case. (The steady-state case represents a background in this method of analysis.) The solid line is a close fit estimate from Eq. (4) with $r = 0$, n_e, T_e (and hence $\langle \sigma v \rangle_{II,III}$) fixed. $D_\perp$ is varied until a good fit is obtained. For this particular case $D_\perp = (1.0 \pm 0.7) \times 10^5\ cm^2/s$. The large error is the difficulty with this approach. Besides shot-to-shot variation in the peak heights and the insensitivity of the time history to the $D_\perp$ value, the ionization times are short compared to the time between gatings in all but the lowest T_e discharges ($8 - 12\ eV$). For the data in Fig. 5, $T_e \sim 9\ eV$. When the electron temperature is increased, the ionization times become short such that a difference in the emission profile above background is not noticed after the first gating time. Therefore, this method cannot be used for much of the data. For this particular case $D_\perp$, estimated from the steady-state analysis [Eq (6)], was determined to be $(1.6 \pm 0.4) \times 10^5\ cm^2/s$, establishing qualitative agreement between the two independent methods.

Since the time-dependent technique has been shown to be viable in earlier work [5], it

is instructive to further expound the connection to the steady-state method which will be used throughout this work. In analyzing the time-dependent emission profile it is necessary to include the ubiquitous steady-state emission profile. Since these equations are linearly independent solutions of the same differential equation, their sum is also a solution. We may, then, add the two solutions [Eq. (4) and (6)] to simulate the time-dependent experimental profile data. The one-dimensional profile may be completely specified by a single parameter, $r_{1/2}$ (*the half-width at half-height*). *In* Fig. 6, $r_{1/2}$ *for* CII *is plotted vs. time after firing* the spark probe (335 μs). The open circles represent the experimental data with the error bars indicating the scatter in the value of $r_{1/2}$. The dashed curve through the closed circles represents the resulting $r_{1/2}$ values obtained in the simulation. The analytic trace is in good agreement with the data. Here a value of $D_- = (1.55 \pm 0.54) \times 10^5\ cm^2/s$ was used in the simulation as determined by the method of peak heights described above. The solid line at $r_{1/2} = 1.3\ cm$ is that value for the steady-state emission profiles obtained under similar conditions. A steady-state $D_\perp$ value of $(1.9 \pm 0.6) \times 10^5\ cm^2/s$ was determined from this data. Within the error bars of the measurement, the time dependent and steady-state evaluation of $D_\perp$ are identical. Since the steady-state method may be used over the entire range of plasma parameters in this experiment, it will be the only method considered hereafter.

Before leaving the time-dependent emission behaviour completely, some physical insight into the ionization balanced diffusion problem may be gained by examining Fig. 6 in more detail. Just after firing the spark probe at 335 μs, the emission profile is quite narrow. Since the carbon will have had little time to diffuse from the source, the emission profile *is not very different from that of the source term. As time progresses, the spark injected* carbon profile broadens under the action of diffusion. This happens quite rapidly because of the short gradient scale lengths for diffusion at this time. The half-width becomes larger than that of steady-state, even though the ionization rate is constant. Note that if the ionization rate were zero, the $r_{1/2}$ trace would diverge like $\sqrt{t}$ as can be seen from Eq. (4).

This behaviour is closely followed in Fig. 6 from 335 to 345 μs. After 345 μs ionization becomes more comparable as the gradient scale length is increasing (the CII density profile is flattening). Finally, the profile decays to the equilibrium solution where diffusion is completely balanced by ionization (at $\sim$ 365 μs in Fig. 6). This broadening and peaking behaviour is only observed in low T_e discharges. In high T_e discharges the ionization time for CII becomes too short to notice any profile broadening above the steady-state value of $r_{1,2}$. The $r_{1/2}$ vs. time trace in this case monotonically approaches the steady-state solution.

Returning to the more practical endeavor of finding equilibrium solutions, we note that the solution to Eq. (6) may be written in the form

$$0 = \frac{n_o}{2} - n_o f(D_\perp, r_{1/2}) \quad , \tag{9}$$

where n_o is the peak density and f is the functional form of the density profile viewed as a function of $D_\perp$ and $r_{1/2}$. The procedure for determining $D_\perp$ is to iterate on $D_\perp$ at a fixed $r_{1/2}$ (determined from the experiment) to find the zero of Eq. (9) using the Newton-Raphson method. This method is guaranteed since the right hand side of Eq. 9 is monotonic in $D_\perp$ for a fixed $r_{1/2}$, exhibiting only one zero. Convergence to 1 part in 10^6 is usually obtained in 5 - 10 iterations.

Effects which may lead to distortion of the emission profiles from the analytically expected density profiles, like the inclusion of bulk plasma motion in the rate equation and atomic physics issues of recombination and non-uniform plasma parameter profiles, were investigated by numerical solution to the coupled species rate equations[18]. For the conditions of the experiment and for reasonable estimates for neutral densities, these effects were seen to make negligible contribution to the emissivity profiles.

3.4. Error Analysis

Sources of error in this analysis stem from 1) uncertainties in the plasma parameters n_e and T_e which affect D_- through the ionization rates; 2) uncertainties in electron impact ionization cross sections, σ_{eii}, given in the literature[15,19]; and 3) uncertainties in the measured values r_o and $r_{1/2}$ which affect the interpretation of the emission profile and, hence, D_-. The standard error in the recommended cross-section data is claimed to be $\sim 10\%$ [19]. In the case of n_e and T_e, the single shot uncertainty may be as high as 30% or greater. However, since we have many shots at similar plasma conditions, we may employ shot averaging of individual Thomson scattering wavelength channels to reduce the uncertainties in n_e and T_e to $\sim 10\%$ in most cases. This is a significant improvement over the method of arithmetic averaging of the n_e and T_e values attained on each shot, which does not improve counting statistics and is biased toward higher T_e values by Poisson statistics[20].

In addition to the relative uncertainty in n_e, there is an absolute error associated with calibration assumptions and uncertainties. This is estimated to be $\sim 20\%$.

While errors in σ_{eii} and n_e produce relatively mild uncertainty in $D_\perp$, the uncertainty produced by errors in T_e is usually more pronounced. This can be easily understood by noting the strong dependence of $\langle \sigma v \rangle$ on T_e, especially when $T_e \lesssim E_I$. For example as T_e ranges from 5 to 10 eV, $\langle \sigma v \rangle_{11,111}$ ranges over two orders of magnitude. Fortunately, we are seldom on this very low temperature range and the uncertainty in T_e is typically $\lesssim 10\%$, thus keeping the resultant $D_\perp$ uncertainties to acceptable levels.

There is also an uncertainty in the source width, r_o, which leads to error in $D_\perp$. The possible range of r_o values can be estimated from source profiles like that of Fig. 4. From this we find $r_o = (0.83 \pm 0.1)\ cm$.

Similarly, there are errors in experimentally determining the $r_{1/2}$ values. The source of these uncertainties is shot-to-shot reproducibility and photoelectron counting statistics. The

Table 1: Average Parameters for an 8 kV Discharge at 335 μs

Parameter	Value	Units	% error in $D_\perp$
T_e	10.0 ± 0.45	eV	12.3
n_e (relative)	7.0 ± 0.4	$10^{13}\ cm^{-3}$	5.7
n_e (absolute)	7.0 ± 1.4	$10^{13}\ cm^{-3}$	19.4
r_o	0.83 ± 0.1	cm	23.4
$r_{1/2}$	1.23 ± 0.06	cm	19.6
$(\sigma v)_{H,H}$	0.2 ± 0.02	$10^{-8}\ cm^3/s$	11.0

latter is relatively unimportant in this context. Since the count rates are typically several hundred to several thousand counts, the error encountered from photoelectron counting is only a few percent. In addition, shot-to-shot deviation typically introduces another $5 \sim 10\%$ uncertainty in $D_\perp$.

Since all of these sources of relative error may be regarded as independent, they will combine in quadrature (i.e., the relative variances will add). The propagation and accumulation of error is best illustrated by an example. The parameters of concern for the average $8kV$ discharge at 335 μs are given in Table 1 along with their uncertainties and percentage errors they produce in $D_\perp$. These were estimated by recalculating $D_\perp$ using the value $x \pm \sigma$ in place of x where $x = T_e, n_e, r_o, r_{1/2}, \langle \sigma v \rangle$. The effect of each value was checked independently. In quadrature, these errors accumulate to a 40% uncertainty in $D_\perp$. From this we may quote $D_\perp = (1.24 \pm 0.5) \times 10^5\ cm^2/s$.

4. Results and Scaling

4.1. *The Functional Form of D_-*

The functional dependencies of B and T_e in the diffusion coefficient are revealed in an examination of the profiles shown in Fig. 7. The electron temperature for profile 7a and profile 7b are 38 and 63 eV, respectively, while the magnetic field strength and electron density are nearly the same. In addition, the ionization times are approximately equal being $0.89\mu s$ and $0.9\mu s$, respectively. (This is due to the compensating effects of small density change and small rate coefficient change for the large temperature difference.) Since the width of profile 7b is larger than that in profile 7a, 7b has the larger value of $D_- = (2.02 \pm 0.42) \times 10^6\ cm^2/s$ while that of profile 7a is only $(5.0 \pm 1.9) \times 10^5\ cm^2/s$. Thus, there is a strong T_e dependence.

We may proceed in a similar manner for profiles 7c and d which have different magnetic field strengths (920 and 1450 G, respectively), but nearly the same T_e and n_e. Again, the ionization times are similar being 2.7 μs for 7c and 2.1 μs for 7d. Now, however, the profile extent has decreased in going from 7c-d and the diffusion constants are $(3.78 \pm 1.27) \times 10^5\ cm^2/s$ and $(1.86 \pm 0.8) \times 10^5\ cm^2/s$, respectively. Hence, there is an inverse dependence on B.

We now examine the electron density dependence. In the operation of the $S-1$ machine, it is difficult to vary the electron density independently of other parameters. In particular, at constant fill pressure there tends to be an inverse dependence of T_e on n_e. As n_e increases the electron temperature decreases as can be seen in Fig. 8. Consequently, the n_e dependence in D_- may be examined by considering a small window in parameter space in which T_e and B do not vary substantially. Figure 9 is an example of such a window. In this case, $45 < T_e < 65\ eV$ and $2100 < B < 2500\ G$ while n_e varies from $4.5 - 7.5 \times 10^{13}\ cm^{-3}$. In this range, D_- is independent of n_e. Although T_e and B do vary in this window, the ratio $\frac{T_e}{B}$ varies only by $\sim 20\%$ where the range of n_e is $\sim 67\%$.

The result of all the above-mentioned functional dependence analyses results in a scaling relation.

$$D_{\perp} = f(T_e, B) \propto \frac{T_e^a}{B^b} \quad . \tag{10}$$

where the exponents a, b and a constant multiplier are to be determined. To this end, a multiple linear regression analysis has been performed on $D_{\perp}$ with T_e and B as independent variables. In the regression, T_e has the range $8.7 - 63.6\ eV$ and B varies from $920 - 2440\ G$. This results in a scaling

$$D_{\perp} = 6.509 \times 10^6 \frac{T_e^{1.07 \pm 0.25}(eV)}{B^{0.808 \pm 0.4}(G)}\ cm^2/s \quad . \tag{11}$$

Here we have considered data from $t \leq 370\ \mu s$ and from the probe position $r = 42\ cm$. Data from the edge ($r = 33\ cm$) will be discussed in section 4.3. Hence, the scaling presented in Eq. (11) is intended to represent the spheromak central confinement characteristics at times when the plasma is stable to gross MHD modes ($n = 0, 1$). The scaling behaviour is indicated in Fig. 10 where $D_{\perp}$ is plotted against the regression on $D_{\perp}$ [Eq. (11)].

These functional trends are apparent in the emission profile widths. In Fig. 11 the half-width, $r_{1/2}$, minus the source width, r_o, is plotted against T_e for constant $B \sim 2400\ G$ and $n_e \sim 7 \times 10^{13}\ cm^{-3}$. The solid line is $r_{1/2} - r_o$ calculated from Eq. (6) assuming the $D_{\perp}$ scaling of Eq. (11). On the left side of the minimum ($T_e \lesssim 40\ eV$) the behaviour is dominated by ionization since the rate coefficient increases an order of magnitude between $10 - 40\ eV$ and the profile narrows. In the region beyond $40\ eV$, the rate coefficient becomes nearly constant and the curve turns upward, increasing with T_e. Assuming $\langle \sigma v \rangle_{II,III}$ remains constant, this relation would eventually approach $\sqrt{T_e}$.

Some sample values of $D_{\perp}$, $D_{\perp}/D_{Bohm}$, and $D_{\perp}/D_{\perp_{cl}}$ are listed in Table 2 along with relevant plasma parameters where

$$D_{Bohm} = \frac{10^8}{16} \frac{T_e(eV)}{B(G)}\ cm^2/s \tag{12}$$

Table 2: Some values for plasma parameters, $D_\perp$, and ratios for an average shot at each condition.

V_{bank}	$n_e(10^{13}cm^{-3})$	$T_e\,(eV)$	$B(G)$	$\ln\Lambda$	$D_\perp\,(\frac{cm^2}{s})$	$\frac{D_\perp}{D_{Bohm}}$	$\frac{D_\perp}{D_{\perp_{cl}}}$
8	10.4	9.7	1060	10.3	2.7×10^5	4.6	1.2
10	9.0	15.6	1420	11.1	3.5×10^5	5.1	4.0
12	7.4	31.0	1860	12.2	5.9×10^5	5.6	17.9
14	6.6	47.5	2460	12.9	7.4×10^5	6.1	51.7

and

$$D_{\perp_{cl}} = 7.1 \times 10^{-4}\,\frac{n_{H^+}(cm^{-3})\ln\Lambda}{\sqrt{T_e(eV)}B^2(G)}\;cm^2/s \tag{13}$$

for Carbon-Hydrogen collisions assuming $T_e = T_i$.

The results $D_\perp$, $5.25 \times D_{Bohm}$, and $D_{\perp_{cl}}$ are plotted in Fig. 12. In all cases, except those at very low T_e, $D_\perp$ is clearly much greater than classical. The tendency for non-classical behaviour persists throughout parameter space and the disparity from $D_{\perp_{cl}}$ increases with T_e. At the same time, the relation to D_{Bohm} holds quite well through the entire range of parameter space.

4.2. T_e, T_{H^+}, T_{CII} Connection

In the discussion of the previous Section, it has been assumed that $T_i = T_e$ in the evaluation of diffusion constant scaling. In reality, the temperature that should appear in $D_{\perp_{cl}}$ is T_{H^+} since the classical transport is driven by $CII - H^+$ collisions. To estimate the relation between T_e and T_i, we determine the mean rate of collisional energy transfer between the species. This can be quantified by considering the equilibration time, $\tau^e_{a/b}$, [21] in *cgs* units

$$\frac{1}{\tau^e_{a/b}} = 1.75 \times 10^{-19}\,\frac{Z_a^2 Z_b^2 n_b(cm^{-3})\ln\Lambda\sqrt{m_a(g)m_b(g)}}{[m_b(g)T_a(eV) + m_a(g)T_b(eV)]^{3/2}}\;,\quad s^{-1}. \tag{14}$$

In low temperature S ~ 1 plasmas (T_e = 10 eV, n_e = 1.0 × 10^{14} cm^{-3}) we find that $\tau^e_{H^+/e}$ = 8.3 μs and τ^e_{CIII/H^+} = 2.3 μs where we have taken lnΛ ~ 12. At these low temperatures it is reasonable to assume temperature equilibration among the species.

At higher temperatures (T_e = 50 eV, n_e = 7.0 × 10^{13} cm^{-3}) we calculate $\tau^e_{H^+/e}$ = 133.0 μs and τ^e_{CIII/H^+} = 38.2 μs where again lnΛ ~ 12. These long equilibration times should not be disconcerting, however. It should be noticed that $\tau^e_{a/b}$ is not a constant. As T_e progresses from low to higher values, $\tau^e_{a/b}$ progresses from very short to moderately long times as $T^{3/2}$. Hence, the ions are able to *keep up* quite well initially. It is only when T_e is very large that classical energy exchange among species is significantly reduced. The result is that *at these moderate electron temperatures, T_i is not expected to be significantly* different from T_e. In addition, there exist anomalous (non-classical) heating mechanisms that produce higher ion temperatures than can be expected classically. In addition, the error introduced in making the approximation T_i = T_e is reduced by the $\sqrt{T}$ dependence in $D_{\perp a}$.

1.3. Time-Resolved Particle Transport and the Relaxation Phenomenon

It has been illustrated[11] that in the S ~ 1 spheromak a *step-wise* relaxation in T_e and j profiles occurs reproducibly in high temperature discharges similar to that first reported on *CTCC* - 1 [22]. It has also been suggested[11] that, concomitant with the relaxation, there is a degradation in confinement. In this Section it will be shown that, although this may be true regarding energy confinement, it is most likely not the case when considering particle confinement. The observation on S ~ 1 is that particle transport is continuously increasing before the relaxation event and does not show a marked increase during the event.

The relaxation scenario as posed in Ref. [11] is as follows. In a high voltage (thus high T_e and B) discharge, transport allows temperature gradients to build in the plasma center, causing the decay time of poloidal flux (due to central toroidal currents) to be larger than

the decay time of toroidal flux (due to edge poloidal currents). This disparity in decay rates forces the spheromak plasma away from the Taylor state since the minimum energy state requires equal decay rates (i.e., self-similar decay). Thus, the implication is that the difference in decay rates is caused by a resistivity profile. The disparity in decay rates produces a poloidal flux rich plasma which moves away from the Taylor state and leads to sudden relaxation. This reproducibly occurs in the $S \sim 1$ plasma 360 – 370 μs after discharge formation.

Hart et al. [23], have investigated deviations from the Taylor state by employing the equilibrium condition

$$\frac{j_\parallel}{B} = I_p'(\psi) + \mu_o \frac{p'(\psi) I_p(\psi)}{B^2} \tag{15}$$

Here, we have used the poloidal current instead of the traditional stream function. The prime denotes differentiation with respect to ψ. The Taylor state of minimum energy requires that $j_\parallel / B$ be a spatial constant (i.e., $\mu = \mu_o \frac{j_\parallel}{B} = const.$). Thus, for this idealized state $I_p(\psi)$ must be a linear function of ψ and $p' = 0$ everywhere. It has been shown[16] that this is the case for previous $S \sim 1$ low temperature plasmas where the only significant pressure gradient is at the edge. In the present experiment, the plasma is in the Taylor state at ~ 310 μs after which pressure gradients are found in the bulk plasma, as can be seen in Fig. 13c where $\kappa = \frac{1}{p}\frac{\partial p}{\partial r}$. Figures 13a,b show the measured $D_\perp$ vs. time for 10 and 14 kV series of discharges, respectively. The circles represent outside data ($r = 33$ cm) and the $x's$ represent inside data ($r = 42$ cm). The heavy dark lines are drawn to aid the eye in following the temporal trends. All the data (save one outside point in the $V = 10$ kV case) fall within these two guide lines.

There are four topics of interest in Fig.13. Firstly, the temporal behaviour of $D_\perp$ follows that of κ quite closely in the time interval 300 – 400 μs. This indicates the influence of pressure gradients causing deviations from the Taylor state and enhancing particle transport. Secondly, the effect of pressure gradients is observed in both the low ($V = 10$ kV) and the

high ($V = 14\ kV$) current discharges. In both cases pressure gradients exist in the plasma while $I_p'(\psi)$ deviations from linearity only exist in the latter case. As well, relaxation events only exist in the latter case. Thirdly, the inside ($r = 42\ cm$) and outside ($r = 33\ cm$) data agree qualitatively (showing the same temporal trend), indicating that the transport mechanism is not localized. Occasionally, there exists a larger diffusion constant for the outside data. It is conjectured that higher fluctuation levels in the plasma periphery, existing throughout much of the discharge, may lead to enhanced diffusion by mixing parallel and perpendicular particle transport. This is also a possible explanation for the large diffusion rates early in the discharge during a period of violent magnetic activity following formation. Fourthly, there is no sudden increase in the particle transport rate near the relaxation time ($\sim 370\ \mu s$) in the $14\ kV$ case. Rather, the particle transport rate builds as the pressure gradient increases in the plasma ($300 - 370\ \mu s$). The relaxation phenomenon suddenly flattens the T_e profile. This is indicated by a lower κ value after $370\ \mu s$ as shown in Fig. 13c. The particle transport rate then decreases following the drop in ∇p rather than showing a sudden increase as would be expected in a step-wise particle loss occurring at the relaxation time.

One possible physical picture is that the relaxation, happening on a short reconnection time scale, allows for a large amount of electron thermal conduction energy loss from the plasma center to the periphery which can occur on open field lines during the reconnection. Thus, the T_e profile may quickly flatten. However, the transport of massive ions, occurring on the much longer sound time, cannot occur to substantial proportions in the reconnection time period.

The preceding scenario could be qualitatively verified by some simple arguments. The reconnection time may be estimated[24] as

$$\tau_x \sim \tau_R^{3/5} \tau_A^{2/5} \quad , \tag{16}$$

where $\tau_R = \mu_o L^2/\eta$ is the resistive decay time and $\tau_A = a(\frac{B}{\sqrt{\mu_o n_i m_i}})^{-1}$ is the Alfvén transit

time. During the reconnection we can estimate the radial thermal conductivity as being enhanced in proportion to the mean square stochastic field amplitude[25] such that $\kappa_r \sim (\frac{\delta B}{B})^2 \kappa_{\parallel e}$. The thermal transport time can then be estimated

$$\tau_T = a^2 (\frac{B}{\delta B})^2 \frac{m_e}{3.2 T_e \tau_{ee}} \quad , \tag{17}$$

where τ_{ee} is the electron-electron collision time. We can proceed similarly for the mean diffusion time but now noting that mass transport will occur at the sound speed $\sim \sqrt{T_e/m_i}$. So that the diffusion time is obtained

$$\tau_D = a^2 (\frac{B}{\delta B})^2 \frac{m_i}{T_i \tau_{ii}} \quad , \tag{18}$$

where it has again been assumed that $T_i = T_e$. For typical plasma conditions $\tau_R \sim 200\ \mu s, T_e = 50\ eV, n_e = 5 \times 10^{19}\ m^{-3}, B = 0.3\ T, \frac{\delta B}{B} \sim 0.02$, and $a = 0.1\ m$ the following times are computed $\tau_A = 0.1\ \mu s, \tau_x = 9.6\ \mu s, \tau_T = 5.9\ \mu s$, and $\tau_D = 480\ \mu s$. So we see the previously assumed ordering holds $\tau_x \sim \tau_T \ll \tau_D$.

5. Summary and Conclusions

We have demonstrated the extrapolation of a novel measurement technique to higher plasma temperatures. In this way, we are able to attain estimates of the transport quantity $D_\perp$ in the $S = 1$ spheromak. Interpretation of CII emission profiles is dependent on ionization and, therefore, accurate estimates of the local n_e and T_e are necessary. These were provided by Thomson scattering.

Interpretation of the emission profiles follows from direct solution of the impurity continuity equation. Species density profiles may be directly related to emissivity profiles since n_e and T_e have no strong gradients over the spatial extent of emission. Furthermore, the effects of recombination, including charge exchange, are negligible.

Over the modest range of plasma parameters investigated, we have found a Bohm-like dependence for the measured diffusion coefficient. More specifically, the relation $D_\perp \sim$

$5.25 \times D_{Bohm}$ represents all our data quite well. In addition, no density dependence is observed. We have also demonstrated a correlation between $D_\perp$ and plasma pressure gradients following the temporal evolution of the discharge. Finally, the enhanced transport appears to be universal, and the relaxation event[11] may not be responsible for enhanced particle transport.

ACKNOWLEDGEMENTS

This work was performed under the support of US DOE contract number # DE-AC02-76-CHO-3073.

References

[1] ROSENBLUTH, M. N. and BUSSAC, M. N., Nucl. Fusion **19** (1979) 489.

[2] TAYLOR, J. B., Phys. Rev. Lett. **33** (1974) 1139.

[3] TAYLOR, J. B., Relaxation of Toroidal Discharges, in *Pulsed High Beta Plasmas*, edited by EVANS, D. E., page 59, Pergamon Press, New York, 1976.

[4] TAYLOR, J. B., Reviews of Modern Physics **58** (1986) 741.

[5] LEVINTON, F. M. and MEYERHOFER, D. D., Rev. Sci. Instrum. **58** (1987) 1393.

[6] MEYERHOFER, D. D., LEVINTON, F. M., and YAMADA, M., Phys. Rev. Lett. **60** (1988) 933.

[7] ELLIS, Jr., R. A., JANOS, A., JOYCE, J., and YAMADA, M., in *Proceedings of the Fifth Symposium on the Physics and Technology of Compact Toroids*, pages 39–45, Mathematical Sciences Northwest, Bellevue Washington, 1983, 1982.

[8] YAMADA, M., ELLIS, JR., R., FURTH, H. P., HART, G., JANOS, A., JARDIN, S., LEVINTON, F., MEYERHOFER, D., MIMURA, M., NAM, C. H., PAUL, S., SPERDUTI, A., VON GOELER, S., WYSOCKI, F., and YOUNG, P., Initial Results from S – 1 Spheromak, in *Plasma Physics and Controlled Nuclear Fusion Research, 1984*, volume 2, page 535, IAEA, Vienna, 1985, London Conference.

[9] JANOS, A., Phys. Fluids **29** (1986) 3342.

[10] JARDIN, S. and CHRISTENSEN, U., Nucl. Fusion **21** (1981) 1665.

[11] ONO, Y., ELLIS, Jr., R. A., JANOS, A. C., LEVINTON, F. M., MAYO, R. M., MOTLEY, R. W., UEDA, Y., and YAMADA, M., Relaxation Phenomenon in the High Temperature S – 1 Spheromak, Technical Report 2520, PPPL, 1988, submitted to Phys. Rev. Lett.

[12] MAYO, R. M., LEVINTON, F. M., MEYERHOFER, D. D., PAUL, S., UEDA, Y., and YAMADA, M., Spatial and Temporal Behavior of Hydrogen and Carbon in the S – 1 Spheromak, in *Proceedings of the Eighth Compact Toroid Symposium and Ninth U.S. Japan Workshop on Compact Toroids*, page 69, University of Maryland, 1987.

[13] LEVINTON, F. M. and NAVRATIL, G. A., Rev. Sci. Instrum. **54** (1983) 35.

[14] LEVINTON, F. M., MEYERHOFER, D. D., MAYO, R. M., and YAMADA, M., Confinement and Power Balance in the S – 1 Spheromak, to be published, 1988.

[15] BELL, K. L., GILBODY, H. B., HUGHES, J. G., KINGSTON, A. E., and SMITH, F. J., J. Phys. Chem. Ref. Data **12** (1983) 891.

[16] HART, G. W., JANOS, A., MEYERHOFER, D. D., and YAMADA, M., Phys. Fluids **29** (1986) 1994.

[17] ABRAMOWITZ, M. and STEGUN, I. A., editors, *Handbook of Mathematical Functions*, Dover Publications, Inc., New York, 1972.

[18] HULSE, R. A., Nucl. Tech./Fusion **3** (1982) 259.

[19] PHANEUF, R. A., JANEV, R. K., and PINDZOLA, M. S., Atomic Data for Fusion Vol. V: Collisions of Carbon and Oxygen Ions with Electrons, H, H_2, and He, ORNL 6090/V5, Oak Ridge National Laboratory, 1987.

[20] HART, G. W., LEVINTON, F. M., and MCNEILL, D. H., Rev. Sci. Instrum. **57** (1986) 2218.

[21] HINTON, F. L., Collisional Transport in Plasma, in *Handbook of Plasma Physics, Vol. 1 Basic Plasma Physics*, edited by GALEEV, A. A. and SUDAN, R. N., page 148, North-Holland Publishing Co., Amsterdam, 1983.

[22] UYAMA, T., HONDA, Y., NAGATA, M., NISHIKAWA, M., OZAKI, A., SATOMI, N., and WATANABE, K., Nucl. Fusion **27** (1987) 799.

23] HART, G. W., CHIN-FATT, C., DESILVA, A. W., GOLDENBAUM, G. C., HESS, R., and SHAW, R. S., Phys. Rev. Lett. **51** (1983) 1558.

24] FURTH, H. P., KILLEEN, J., and ROSENBLUTH, M. N., Phys. Fluids **6** (1963) 459.

25] RECHESTER, A. B. and ROSENBLUTH, M. N., Phys. Rev. Lett. **40** (1978) 38.

Figures

Fig. 1 Schematic of the S – 1 device showing the carbon injection diagnostic (not to scale). Funnel stabilizers not shown.

Fig. 2. Setup of the carbon injection experiment showing the relationship of the injection probe and coupling optics to the spheromak plasma.

Fig. 3. a) Spectral emission trace in the range of 4200 Å to 4825 Å for a typical $14kV$ carbon injection plasma with background subtracted. The probe position is $R = 42\ cm$ and the line of sight for this channel intersects the midplane at $R = 42.5\ cm$. b) Spectral emission trace for the same plasma conditions with the probe removed. Notice the change of scales.

Fig. 4. Radial emission profile for CII at 4267 Å. Dashed line is a gaussian fit to the raw data with $r_a = 0.83\ cm$.

Fig. 5. Peak of the CII (4267Å) emission profile vs. time after plasma initiation. The spark probe was discharged at 250 μs (open circles). The x's are the steady-state profile peaks under the same conditions.

Fig. 6. Time evolution of $r_{1/2}$ for CII. Open circles are the experimental half-widths for several 8 kV discharges. The x's and dashed line are the results of the simulation using the experimentally determined $D_\perp$ by the method of peak heights. The solid line represents the $r_{1/2}$ value found from the steady-state emission profiles.

Fig. 7. Example CII steady-state emission profiles (solid lines) overlaid by best fits to Eq. (6) (dashed lines).

Fig. 8. n_e as a function of T_e for all the $r = 42\ cm$ data showing an inverse dependence.

Fig. 9. $D_\perp$ dependence on n_e for the small parameter space window $T_e = 45 - 65\ eV, B = 2100 - 2500\ G$.

Fig. 10. D_- scaling behaviour. D_- is plotted against the regression on D_- Eq. (11) for the entire data set consistent with $t \leq 370\ \mu s$ and $r = 42\ cm$. V indicates the operational bank voltage.

Fig. 11. Half-width $r_{1/2} \quad r_o$ vs. T_e for $B \sim 2400\ G$, $n_e \sim 7 \times 10^{13}\ cm^{-3}$.

Fig. 12. The values $D_-(\bullet's)$, $5.25 \times D_{Bohm}(\circ's)$, and $D_{\perp cl}(\triangle's)$ vs. T_e.

Fig. 13. Time resolved particle transport and pressure gradients in $S = 1$ plasmas. a) measured D_- vs. time for a V = 10 kV case. b) measured D_- vs. time for a V = 14 kV case. c) inverse pressure gradient scale length $\kappa = \frac{1}{p}\frac{\partial p}{\partial r}$ for a V = 14 kV case.

EXPERIMENTAL SETUP:
CARBON INJECTION EXPERIMENT

88X0627

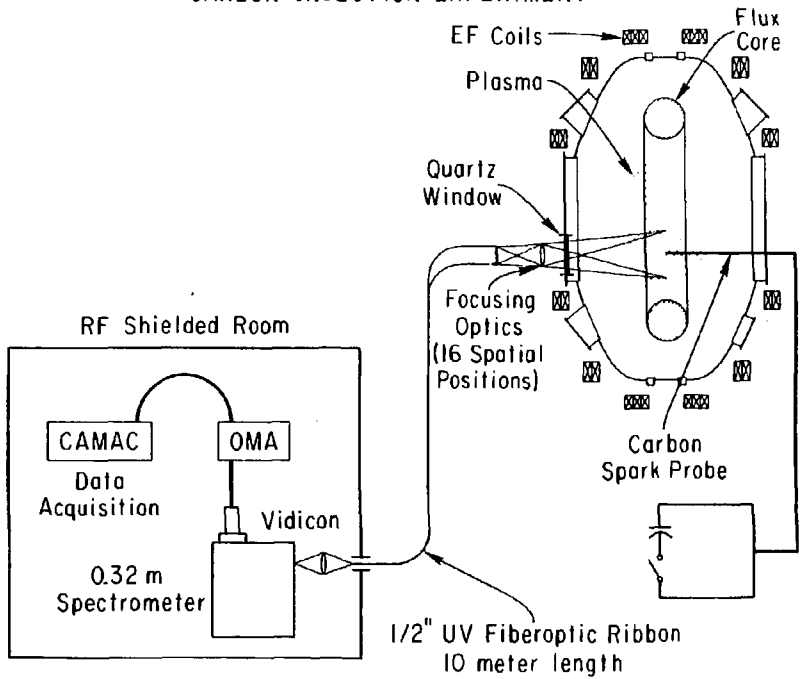

Fig. 1

DETAILED VIEW OF SPARK EXPERIMENT SETUP

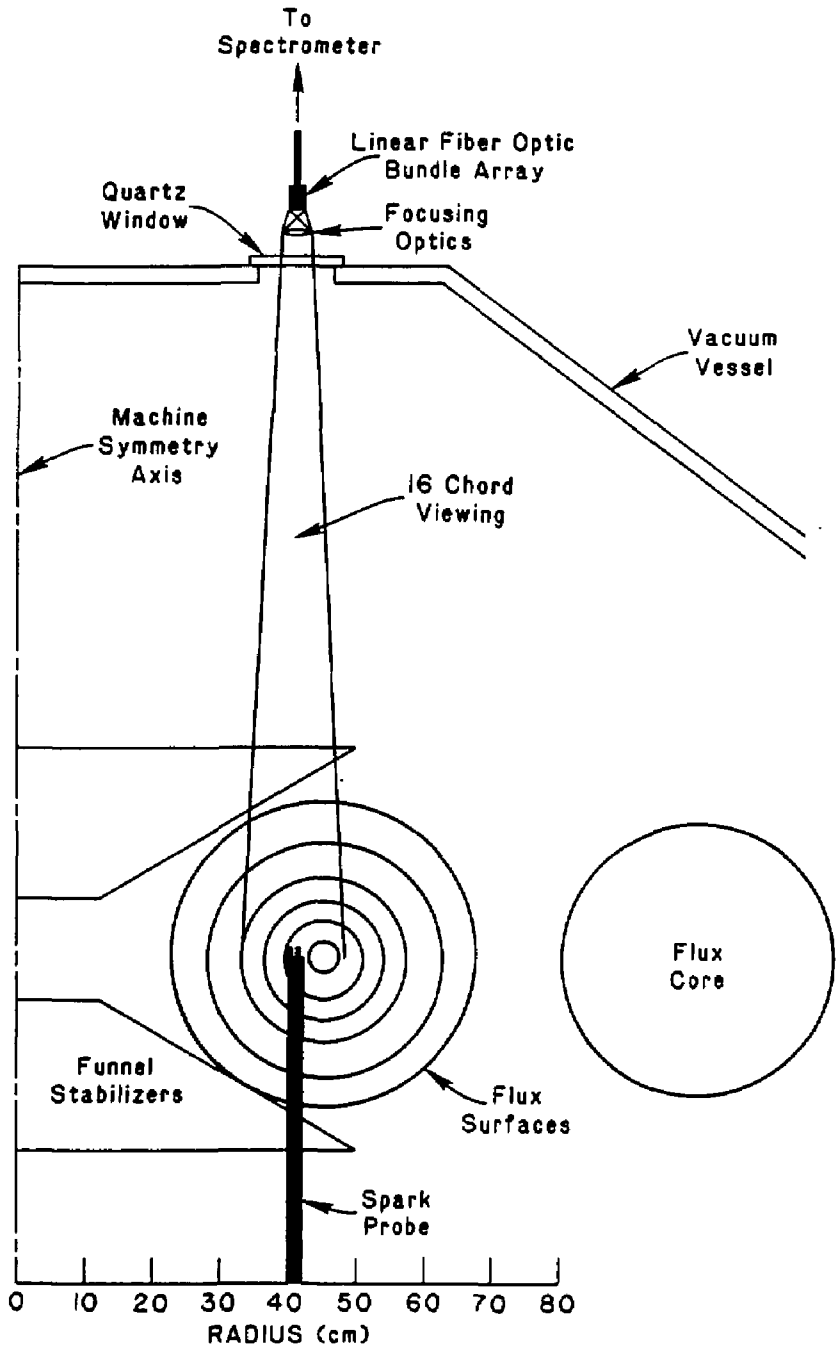

Fig. 2

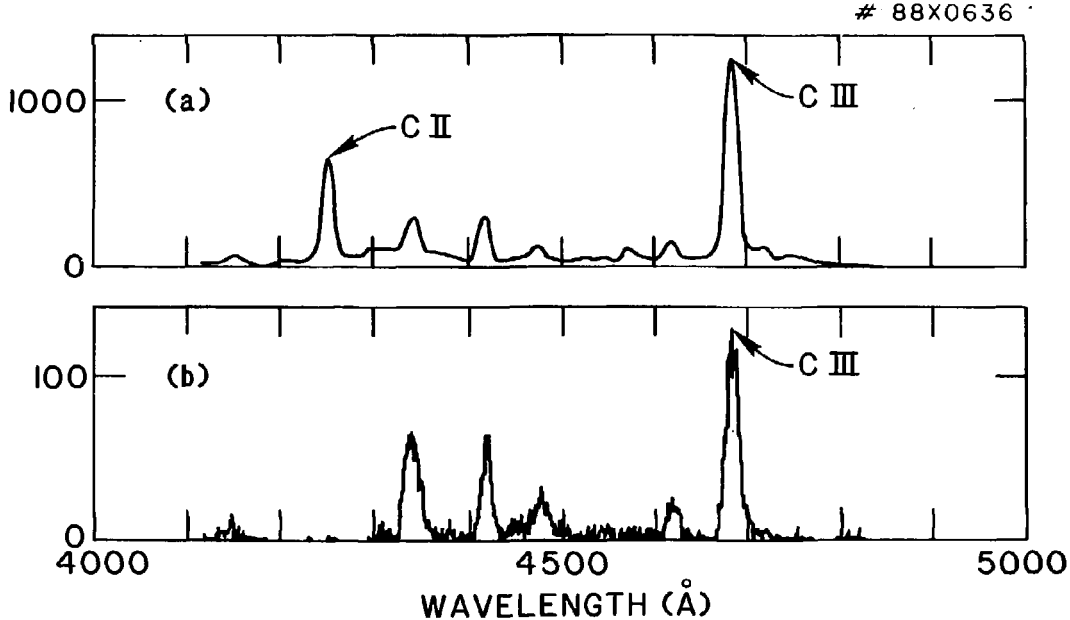
88X0636
1000
(a)
C II
C III
0
100
(b)
C III
0
4000
4500
5000
WAVELENGTH (Å)

Fig. 3

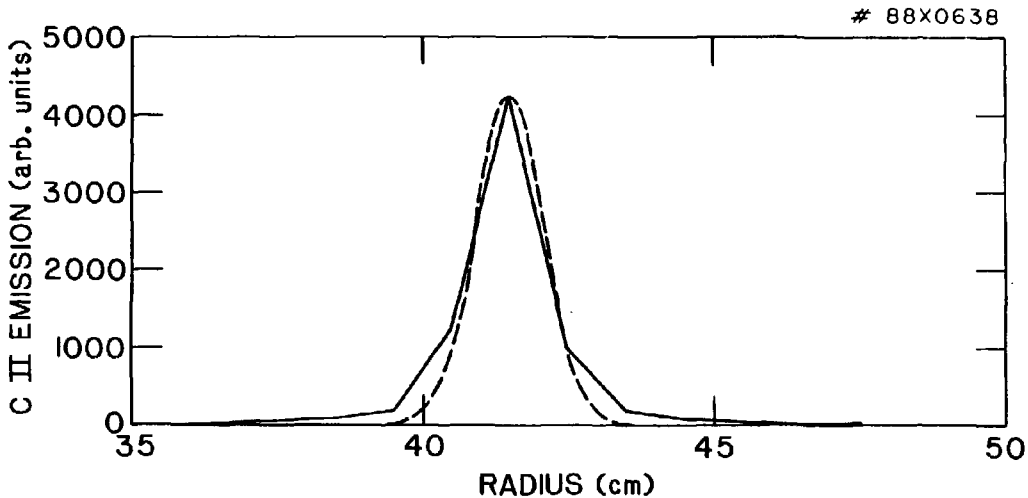
88X0638
C III EMISSION (arb. units)
5000
4000
3000
2000
1000
0
35
40
45
50
RADIUS (cm)

Fig. 4

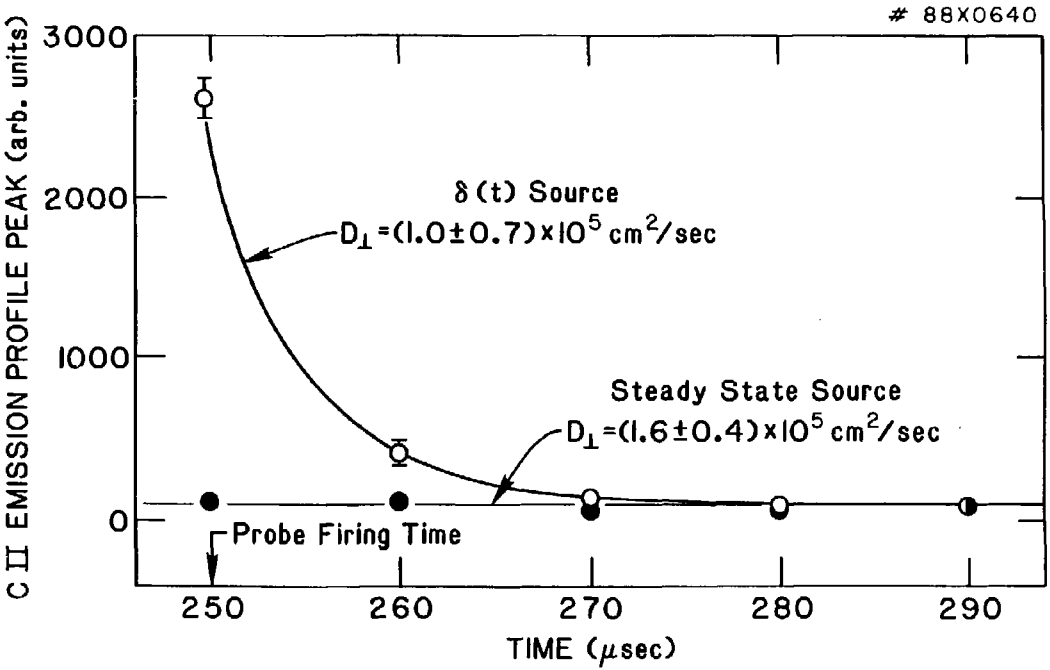
88X0640
C II EMISSION PROFILE PEAK (arb. units)
3000
2000
1000
0
δ(t) Source
$D_\perp = (1.0 \pm 0.7) \times 10^5$ cm^2/sec
Steady State Source
$D_\perp = (1.6 \pm 0.4) \times 10^5$ cm^2/sec
Probe Firing Time
250
260
270
280
290
TIME (μsec)

Fig. 5

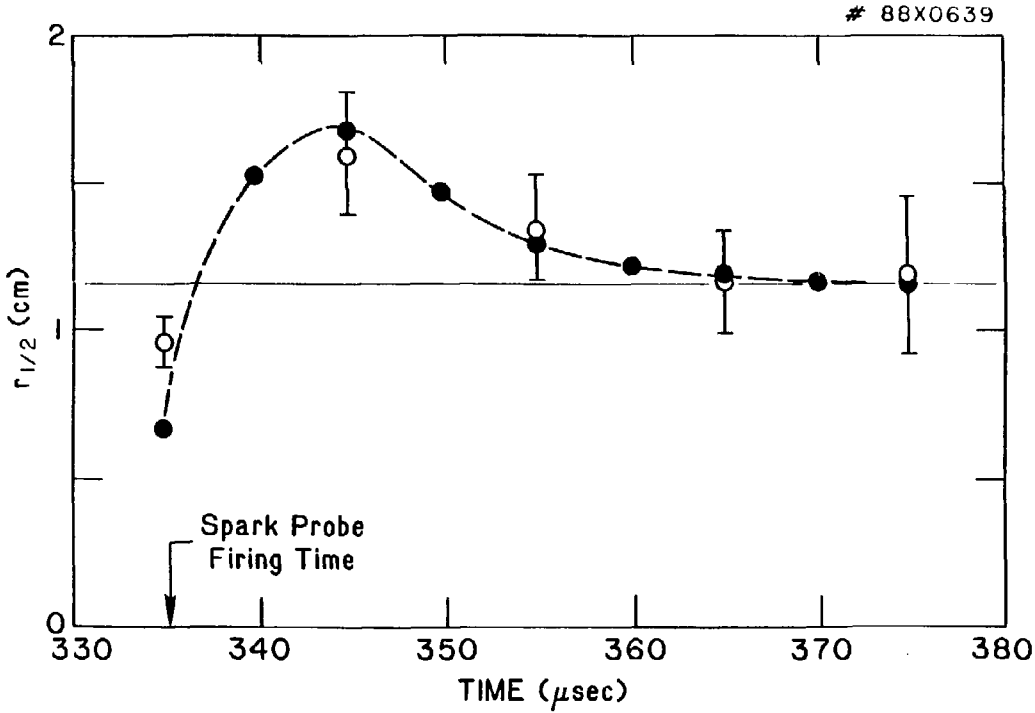
88X0639
2
1
0
$r_{1/2}$ (cm)
Spark Probe
Firing Time
330
340
350
360
370
380
TIME (μsec)

Fig. 6

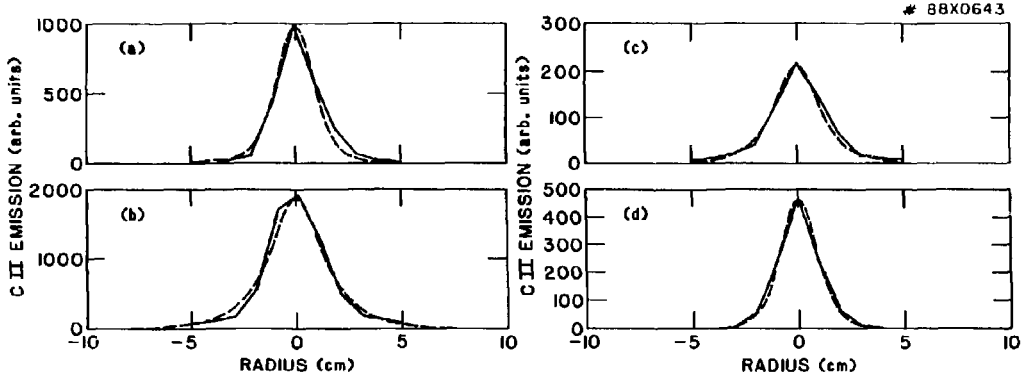
88X0643
(a)
(b)
(c)
(d)
C III EMISSION (arb. units)
C III EMISSION (arb. units)
RADIUS (cm)
RADIUS (cm)
1000
500
0
2000
1000
0
300
200
100
0
500
400
300
200
100
0
-10
-5
0
5
10

Fig. 7

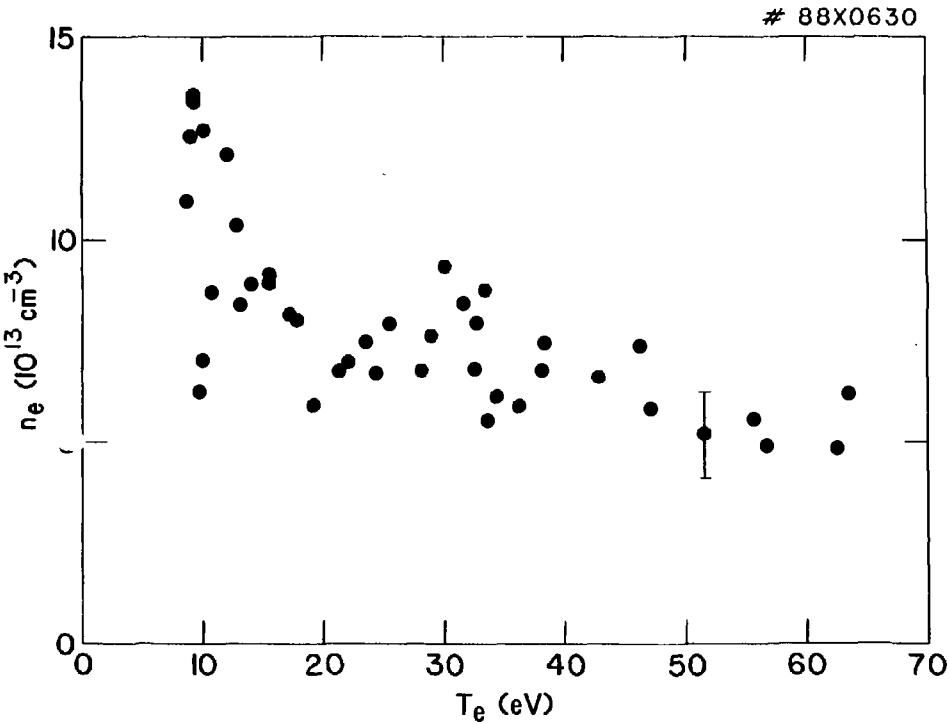

Fig. 8

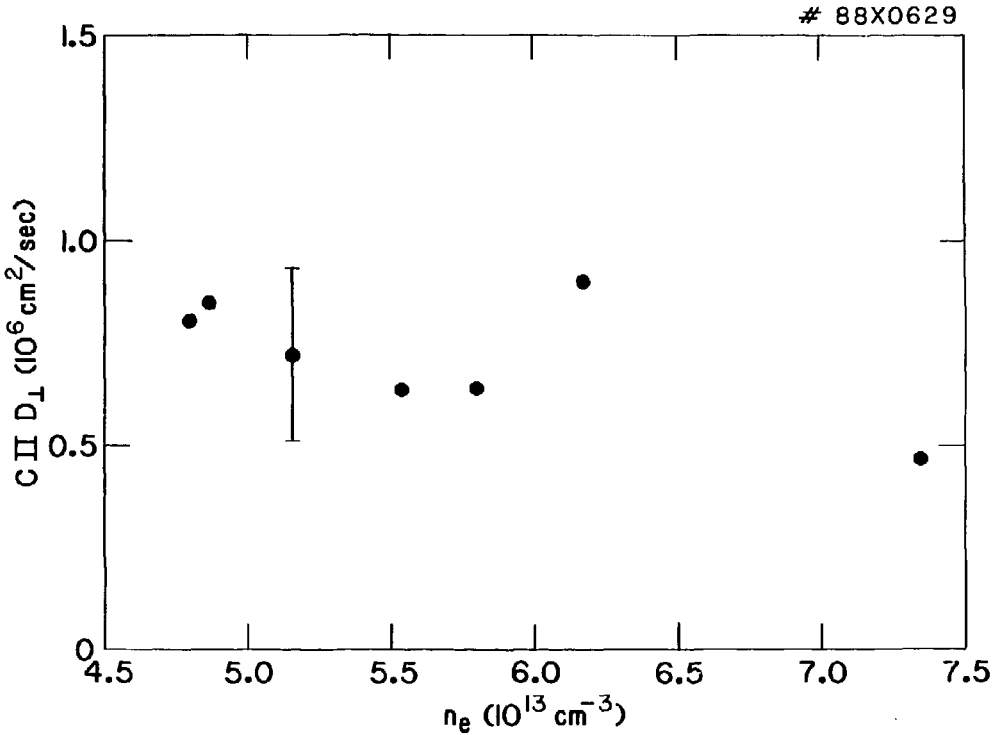
88X0629
1.5
1.0
0.5
0
C II $D_\perp$ (10^6 cm^2/sec)
4.5
5.0
5.5
6.0
6.5
7.0
7.5
n_e (10^{13} cm^{-3})

Fig. 9

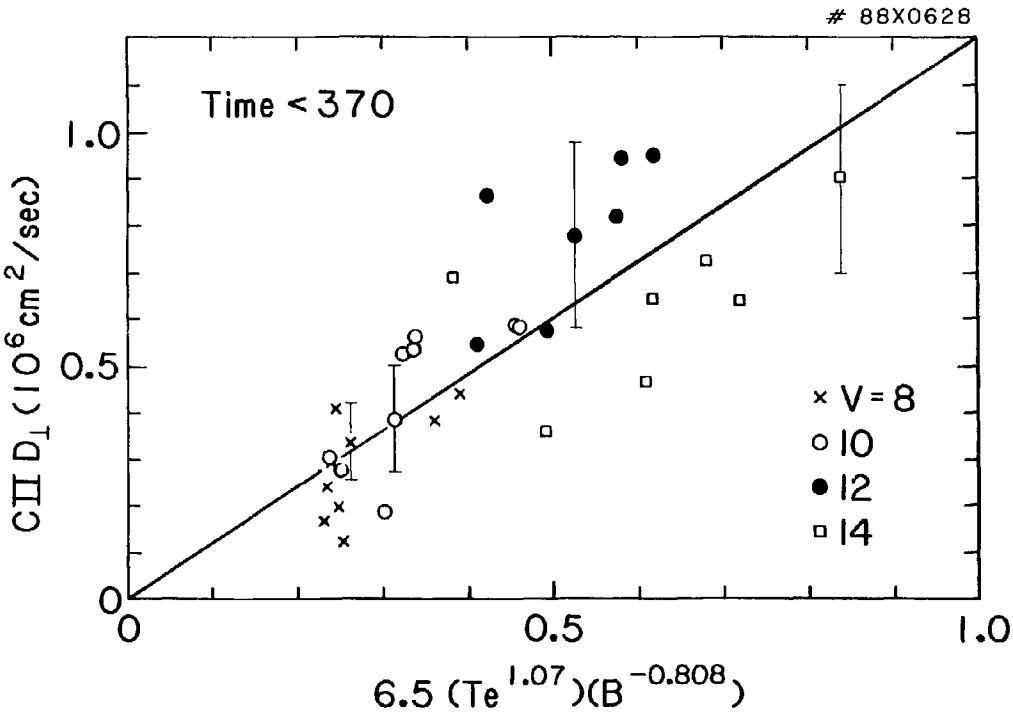
88X0628
Time < 370
1.0
0.5
0
0
0.5
1.0
CII $D_\perp$ ($10^6 cm^2/sec$)
6.5 ($Te^{1.07}$)($B^{-0.808}$)
× V = 8
○ 10
● 12
□ 14

Fig. 10

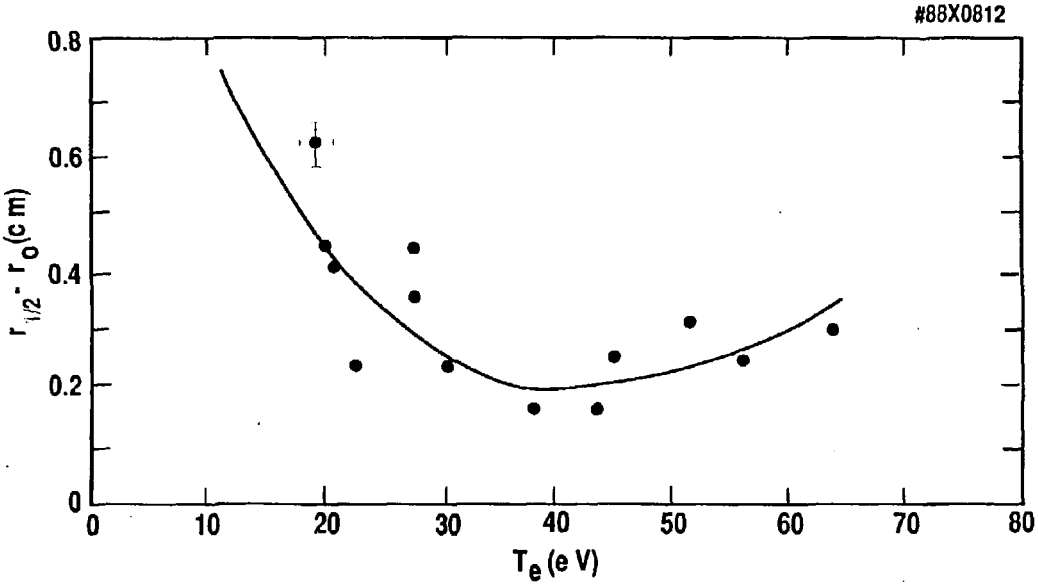

Fig. 11

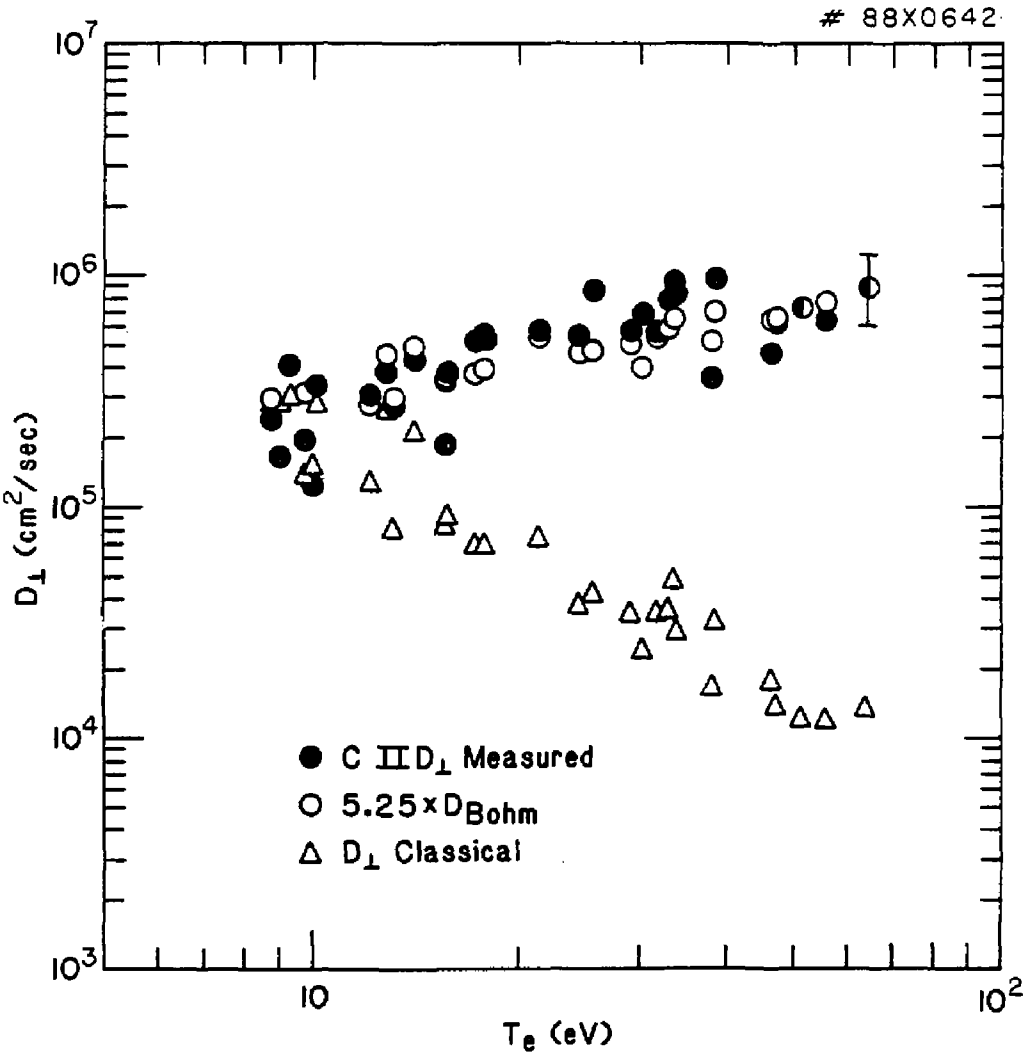
88X0642
10^7
10^6
10^5
10^4
10^3
$D_\perp$ (cm^2/sec)
● C III $D_\perp$ Measured
○ 5.25×D_{Bohm}
△ $D_\perp$ Classical
10
10^2
T_e (eV)

Fig. 12

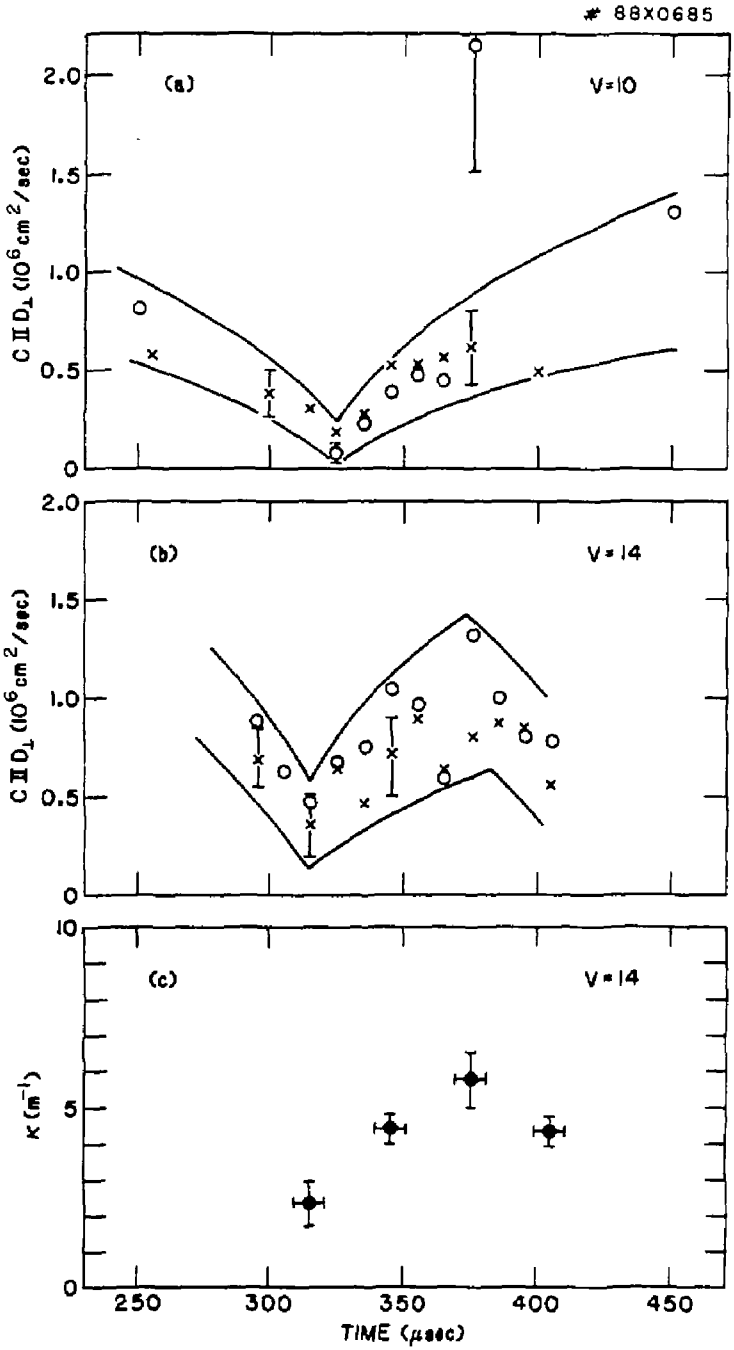
88X0685
(a)
V=10
(b)
V=14
(c)
V=14
$C_{\perp}D_{\perp}$ (10^6 cm^2/sec)
$C_{\perp}D_{\perp}$ (10^6 cm^2/sec)
κ (m^{-1})
TIME (μsec)
0
0.5
1.0
1.5
2.0
5
10
250
300
350
400
450

Fig. 13

EXTERNAL DISTRIBUTION IN ADDITION TO UC-20

Dr. Frank J. Paoloni, Univ of Wollongong, AUSTRALIA
Prof. M.H. Brennan, Univ Sydney, AUSTRALIA
Plasma Research Lab., Australian Nat. Univ., AUSTRALIA
Prof. I.R. Jones, Flinders Univ., AUSTRALIA
Prof. F. Cap, Inst Theo Phys, AUSTRIA
Prof. M. Heindler, Institut fur Theoretische Physik, AUSTRIA
M. Goossens, Astronomisch Instituut, BELGIUM
Ecole Royale Militaire, Lab de Phys Plasmas, BELGIUM
Commission-European, Dg-XII Fusion Prog, BELGIUM
Prof. R. Boucique, Laboratorium voor Natuurkunde, BELGIUM
Dr. P.H. Sakanaka, Instituto Fisica, BRAZIL
Instituto De Pesquisas Especiasi-INPE, BRAZIL
Documents Office, Atomic Energy of Canada Limited, CANADA
Dr. M.P. Bachynski, MPB Technologies, Inc., CANADA
Dr. H.M. Skarsgard, University of Saskatchewan, CANADA
Dr. H. Barnard, University of British Columbia, CANADA
Prof. J. Teichmann, Univ. of Montreal, CANADA
Prof. S.R. Sreenivasan, University of Calgary, CANADA
Prof. Tudor W. Johnston, INRS-Energie, CANADA
Dr. C.R. James, Univ. of Alberta, CANADA
Dr. Peter Lukac, Komenskeho Univ, CZECHOSLOVAKIA
The Librarian, Culham Laboratory, ENGLAND
The Librarian, Rutherford Appleton Laboratory, ENGLAND
Mrs. S.A. Hutchinson, JET Library, ENGLAND
C. Mouttet, Lab. de Physique des Milieux Ionises, FRANCE
J. Radet, CEN/CADARACHE - Bat 506, FRANCE
Univ. of Ioannina, Library of Physics Dept. GREECE
Dr. Tom Mual, Academy Bibliographic Ser., HONG KONG
Preprint Library, Hungarian Academy of Sciences, HUNGARY
Dr. B. Dasgupta, Saha Inst of Nucl. Phys., INDIA
Dr. P. Kaw, Institute for Plasma Research, INDIA
Dr. Philip Rosenau, Israel Inst. Tech, ISRAEL
Librarian, Int'l Ctr Theo Phys, ITALY
Prof. G. Rostagni, Univ Di Padova, ITALY
Miss Clelia De Palo, Assoc EURATOM-ENEA, ITALY
Biblioteca, Instituto di Fisica del Plasma, ITALY
Dr. H. Yamato, Toshiba Res & Dev, JAPAN
Prof. I. Kawakami, Atomic Energy Res. Institute, JAPAN
Prof. Kyoji Nishikawa, Univ of Hiroshima, JAPAN
Direc. Dept. Large Tokamak Res. JAERI, JAPAN
Prof. Satoshi Itoh, Kyushu University, JAPAN
Research Info Center, Nagoya University, JAPAN
Prof. S. Tanaka, Kyoto University, JAPAN
Library, Kyoto University, JAPAN
Prof. Nobuyuki Inoue, University of Tokyo, JAPAN
S. Mori, JAERI, JAPAN
Librarian, Korea Advanced Energy Res. Institute, KOREA
Prof. D.I. Choi, Adv. Inst Sci & Tech, KOREA
Prof. B.S. Liley, University of Waikato, NEW ZEALAND
Institute of Plasma Physics, PEOPLE'S REPUBLIC OF CHINA
Librarian, Institute of Phys., PEOPLE'S REPUBLIC OF CHINA
Library, Tsing Hua University, PEOPLE'S REPUBLIC OF CHINA
Z. Li, Southwest Inst. Physics, PEOPLE'S REPUBLIC OF CHINA
Prof. J.A.C. Cabral, Inst Superior Tecnico, PORTUGAL
Dr. Octavian Petrus, AL I CUZA University, ROMANIA
Dr. Johan de Villiers, Fusion Studies, AEC, SO AFRICA
Prof. M.A. Hellberg, University of Natal, SO AFRICA
C.I.E.M.A.T., Fusion Div. Library, SPAIN
Dr. Lennart Stenflo, University of UMEA, SWEDEN
Library, Royal Inst Tech, SWEDEN
Prof. Hans Wilhelmson, Chalmers Univ Tech, SWEDEN
Centre Phys des Plasmas, Ecole Polytech Fed, SWITZERLAND
Bibliotheek, Fom-Inst Voor Plasma-Fysica, THE NETHERLANDS
Dr. D.D. Ryutov, Siberian Acad Sci, USSR
Dr. G.A. Eliseev, Kurchatov Institute, USSR
Dr. V.A. Glukhikh, Inst Electrophysical Apparatus, USSR
Dr. V.T. Tolok, Inst. Phys. Tech. USSR
Dr. L.M. Kovrizhnykh, Institute Gen. Physics, USSR
Nuclear Res. Establishment, Julich Ltd., W. GERMANY
Bibliothek, Inst. Fur Plasmaforschung, W. GERMANY
Dr. K. Schindler, Ruhr Universitat Bochum, W. GERMANY
ASDEX Reading Rm, IPP/Max-Planck-Institut fur Plasmaphysik, W. GERMANY
Librarian, Max-Planck Institut, W. GERMANY
Prof. R.K. Janev, Inst Phys, YUGOSLAVIA